

The feasibility of weak lensing and 21cm intensity mapping cross-correlation measurements

Anut Sangka^{1,2,3}[★] and David Bacon¹

¹*Institute of Cosmology and Gravitation, University of Portsmouth, Portsmouth PO1 3FX, UK*

²*National Astronomical Research Institute of Thailand, Chiangmai 50180, Thailand,*

³*Department of Physics, Faculty of Science, Ubon Ratchatani University, Ubon Ratchatani 34190, Thailand*

Accepted XXX. Received YYY; in original form ZZZ

ABSTRACT

One of the most promising probes to complement current standard cosmological surveys is the HI intensity map, i.e. the distribution of temperature fluctuations in neutral hydrogen. In this paper we present calculations of the 2-point function between HI (at redshift $z < 1$) and lensing convergence (κ). We also construct HI intensity maps from N-body simulations, and measure 2-point functions between HI and lensing convergence. HI intensity mapping requires stringent removal of bright foregrounds, including emission from our galaxy. The removal of large-scale radial modes during this HI foreground removal will reduce the HI-lensing cross-power spectrum signal, as radial modes are integrated to find the convergence; here we wish to characterise this reduction in signal. We find that after a simple model of foreground removal, the cross-correlation signal is reduced by $\sim 50\text{--}70\%$; we present the angular and redshift dependence of the effect, which is a weak function of these variables. We then calculate S/N of κ HI detection, including cases with cut sky observations, and noise from radio and lensing measurements. We present Fisher forecasts based on the resulting 2-point functions; these forecasts show that by measuring $\kappa\Delta T_{\text{HI}}$ correlation functions in a sufficient number of redshift bins, constraints on cosmology and HI bias will be possible.

Key words: Radio lines: General, Gravitational Lensing: Weak, Large Scale Structure of Universe

1 INTRODUCTION

The clustering of matter in the Universe provides an important insight into the origins and evolution of the cosmic structure. Inflation predicts that early structure formation generates a near-Gaussian random field in overdensity; evolution due to gravity causes late-time large-scale structures to exhibit non-Gaussian features. Two point statistics of the density field at different redshifts capture information about the evolution of structures, and correlation functions between different pairs of cosmological probes can precisely constrain cosmological parameters (Abbott et al. 2018; Tröster et al. 2022; Pandey et al. 2021; Fang et al. 2022; Upham et al. 2019). Two dimensional surveys of the cosmic microwave background (CMB) have been effectively carried out through the last few decades (Planck Collaboration et al. 2018; Hinshaw et al. 2013). The complement to this is deep sky observations of the 3-dimensional galaxy and dark matter fields. While conventional optical and infrared surveys have high angular resolution, long integration times are needed for these to obtain precise redshifts via spectroscopy. In contrast, photometric surveys provide faster redshift capture but less radial resolution (Fernandez-Soto et al. 2001).

To complement the low radial resolution of optical photometric surveys, alternative techniques with higher radial resolution are desirable; radio 21cm intensity mapping is a rapidly developing candidate for this purpose. Unlike most optical surveys, this technique does not measure the brightness of individual objects, but focuses on the larger-scale fluctuations in intensity of the 21cm radio signal from neutral hydrogen (HI). The temperature fluctuations can be used as a tracer for the underlying cosmic density field. This intensity mapping is a complementary technique to a photometric survey, with excellent redshift resolution but lower angular resolution (Bull et al. 2015). Hence, combining HI and optical surveys is potentially valuable, as the two techniques compensate for each other's limitations (Cunnington et al. 2019b; Square Kilometre Array Cosmology Science Working Group et al. 2020).

Recently, HI intensity mapping techniques have been actively developed (Santos et al. 2010; Harker et al. 2010; Mao et al. 2008; The CHIME Collaboration et al. 2022; Wolz et al. 2016; Cunningham et al. 2022). The Canadian Hydrogen Intensity Mapping Experiment (CHIME) (CHIME Collaboration et al. 2022) has provided a detection of HI via cross-correlations with three probes of Large-Scale Structure (LSS), namely luminous red galaxies (LRG), emission line galaxies (ELG), and quasars (QSO) from the eBOSS clustering catalogs at high significant levels, 7.1σ (LRG), 5.7σ

[★] E-mail: anut.sangka@port.ac.uk

(ELG), and 11.1σ (QSO). [Cunnington et al. \(2022\)](#) have detected the correlated clustering between MeerKAT measurements of HI and galaxies from the WiggleZ Dark Energy Survey at 7.7σ significance. Intensity mapping is therefore on its way to becoming an independent observational probe, providing useful information from low to high redshifts, via future surveys with radio telescopes such as MeerKAT ([Poursidou 2017](#); [Poursidou et al. 2017](#); [Spinelli et al. 2022](#)) and the Square Kilometre Array, SKA ([Santos et al. 2015](#)).

The major challenge for the intensity mapping technique is that the foreground signals are much stronger than the cosmic HI brightness temperature, especially due to the galactic plane synchrotron radiation ([Spinelli et al. 2018](#); [Su et al. 2018](#); [Switzer et al. 2013](#)). Hence several studies of 2-point functions between HI and optical ($\Delta_{\text{HI}}\delta_{\text{g}}$) have focused on the impact of foreground removal ([Chapman et al. 2012](#); [Cunnington et al. 2019b](#); [Padmanabhan et al. 2020](#); [Cunnington et al. 2020](#); [Spinelli et al. 2022](#)). The study by [Cunnington et al. \(2019b\)](#) shows that the foreground removal affects 2-point function characteristics, especially when the redshift resolution is broad, as is the case in optical photometric surveys.

There are also numerous optical surveys measuring gravitational lensing shear (γ) which distorts the shape of galaxy images; this is sensitive to density fluctuations of all the matter present along a line of sight, whether baryonic or dark matter. It is therefore of interest to consider the viability of the cross-correlation $\gamma - \delta_{\text{HI}}$, which will be able to be studied using a combination of lensing and IM surveys ([Abbott et al. 2018](#); [Baxter et al. 2019](#); [Hu & Jain 2004](#); [The CHIME Collaboration et al. 2022](#); [CHIME Collaboration et al. 2022](#); [Cunnington et al. 2022](#)). The density projection along the unperturbed light ray trajectory, also known as 'lensing convergence' κ can be considered instead of γ as both share the same statistical properties. The 2-point functions between the pairs of κ and HI could improve cosmological constraints and break degeneracies such as that between HI bias (b_{HI}) and clustering amplitude.

However, removing the HI foreground potentially affects these 2-point statistics, as the foreground removal effectively subtracts large-scale radial modes to which lensing is sensitive. In this paper we will calculate the cross-correlation function between convergence and 21cm intensity mapping, and will explore whether the foreground subtraction significantly hampers the cross-correlation measurement. We also explore whether the foreground removal impacts the viability of cosmological constraints from HI-HI and κ -HI correlations.

To achieve this, we will present theoretical and simulation approaches for calculating the κ -HI signal. We will then consider the effect of foreground removal on the signal, showing that the impact is significant (approximately a factor of 2 in signal reduction) but not lethal. We will then use the Fisher information matrix to make cosmological parameter forecasts for ideal and realistic surveys (including cut sky and the inclusion of telescope-specific noise), deploying the cross-correlation between convergence and intensity mapping, always including the effect of foreground removal. We discuss lensing convergence and HI simulation catalogues in Section 2, including modeling of the 2-point functions. We describe the HI foreground removal and its effect on κ -HI 2-point functions in Section 3. We present our Fisher forecasts for surveys in Section 4, effects of instrumental noise in Section 5 and present our conclusions in Section 6.

2 κ -HI 2-POINT STATISTICS: THEORY AND SIMULATIONS

In this section we discuss the relevant 2-point statistics. We shall start with theoretical calculations of 2-point functions of lensing convergence (κ) and neutral hydrogen intensity maps (HI) in subsection 2.1. We will then discuss the generation of κ catalogues and HI modelling from simulations of the matter overdensity δ . The comparison between theoretical calculations and simulations is shown in subsection 2.2. The simulated HI maps will be used in the next section 3 where the foreground removal will be discussed.

2.1 Modeling the 2-point functions

In this subsection, we describe the modeling of the 2-point functions. We begin by considering how to calculate the observable quantities, namely weak lensing convergence κ and HI temperature fluctuations ΔT_{HI} . We will then turn to the angular cross-power spectra. We denote $\kappa\kappa$ as the power spectra between κ fields, HI^iHI^j as the cross-power spectra between HI fields, and κHI as the cross-power between κ and HI. The dummy indices i and j refer to the i th and j th redshift bins. We will calculate the lensing convergence in an arbitrary direction on the sky \hat{n} using the Born approximation, projecting the matter overdensity δ along an unperturbed ray direction. This can be computed by ([Bartelmann & Schneider 2001](#))

$$\kappa(\chi_s, \hat{n}) = \frac{3\Omega_{\text{m}}H_0^2}{2c^2} \int_0^{\chi_s} d\chi' \frac{\chi'(\chi - \chi')}{\chi} \frac{\delta(\hat{n}, \chi')}{a(\chi')}, \quad (1)$$

where χ is comoving distance, Ω_{m} is the matter density parameter at the present epoch, H_0 is the Hubble parameter today and the subscript s refers to the source plane. For lensing of distributed sources in redshift bins i , the integrand is modified by including a source distribution, so that the integration now becomes

$$\kappa^i(\hat{n}) = \int_0^\infty d\chi' q_{\kappa}^i(\chi') \delta(\hat{n}, \chi'), \quad (2)$$

where the lensing weight is given by

$$q_{\kappa}^i(\chi) = \frac{3\Omega_{\text{m}}H_0^2}{2c^2} \int_0^{\chi_s} \frac{\delta(\hat{n}, \chi')}{a(\chi')} \int_{\chi}^{\infty} d\chi'' \frac{\chi'' - \chi}{\chi} \frac{n_s^i(z(\chi'')) \frac{dz}{d\chi''}}{\bar{n}_s^i}, \quad (3)$$

where $n_s^i(z)$ is the lensing source number density, and \bar{n}_s^i is its average in the i th redshift bin.

HI will be a biased tracer of matter overdensity, so we write $\Delta T_{\text{HI}}(\hat{n}, z) = \bar{T}_{\text{HI}}(z) b_{\text{HI}}(z) \delta(\hat{n}, z)$, where $b_{\text{HI}}(z)$ is the HI bias at a given redshift z and $\bar{T}_{\text{HI}}(z)$ is the average temperature. The projected temperature fluctuation at the i th redshift bin is then

$$\Delta T_{\text{HI}}^i(\hat{n}) = \int_0^{\chi_i} d\chi' q_{\text{HI}}^i(\chi') \delta(\hat{n}, \chi'), \quad (4)$$

where

$$q_{\text{HI}}^i(\chi) = \bar{T}_{\text{HI}}(z(\chi)) b_{\text{HI}}^i(\chi) \frac{n_{\text{HI}}^i(z(\chi)) \frac{dz}{d\chi}}{\bar{n}_{\text{HI}}^i}, \quad (5)$$

where $n_{\text{HI}}^i(z)$ is the HI source number density, and \bar{n}_{HI}^i is its average in the i th redshift bin.

[Battye et al. \(2013\)](#) show that for a given redshift z , $\bar{T}_{\text{HI}}(z)$ can be estimated by

$$\bar{T}_{\text{HI}}(z) = 44\mu\text{K} \left(\frac{\Omega_{\text{HI}}(z)h}{2.45 \times 10^{-4}} \right) \frac{(1+z)^2}{E(z)}, \quad (6)$$

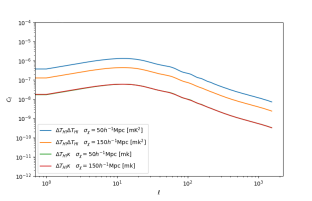


Figure 1. Power spectra C_ℓ for HI and cross-power between HI and convergence, for radial HI width $\sigma_\chi = 50$ and $150 h^{-1}\text{Mpc}$. The effect of the width is less important for the cross-correlation. Different σ_χ corresponds to different frequency bandwidths, $\Delta\nu$ of the radio data.

where $E(z) = H(z)/H_0$ is the dimensionless Hubble function at redshift z . The HI density parameter could be approximated to be $\Omega_{\text{HI}}h = 2.45 \times 10^{-4}$ (Battye et al. 2013). However, throughout this research we shall follow the fitting formula for the SKA-MID I by Square Kilometre Array Cosmology Science Working Group et al. (2020)

$$\Omega_{\text{HI}}(z) = 0.00048 + 0.00039z - 0.000065z^2. \quad (7)$$

Constraining the HI bias $b_{\text{HI}}(z)$ will be discussed later in section 4.

Using the Limber approximation, the angular power spectra $C^{XY}(\ell)$ are given by

$$C^{XY}(\ell) = \int d\chi \frac{q_X(\chi)q_Y(\chi)}{\chi^2} P_\delta\left(\frac{\ell+1/2}{\chi}, z(\chi)\right), \quad (8)$$

where $P_\delta\left(\frac{\ell+1/2}{\chi}, z(\chi)\right)$ is the matter power spectrum (LoVerde & Afshordi 2008). We compute the nonlinear power spectrum using the Boltzmann code CAMB (Lewis & Bridle 2002) with the Halofit extension to nonlinear scales (Takahashi et al. 2012).

Since the ray tracing simulations by Takahashi et al. (2017) which we use below adopt a comoving bin size $\Delta\chi = 150 h^{-1}\text{Mpc}$ (see section 2.2), we choose a radial selection function for $n_{\text{HI}}^i(z(\chi))/\bar{n}_{\text{HI}}^i$ as a normal distribution around a central comoving position with $3\sigma_\chi = 150 h^{-1}\text{Mpc}$. This σ_χ corresponds to the frequency bandwidth ($\Delta\nu$) selected. In practice, the frequency range and bandwidth will depend on the particular radio telescope being used; for example, BINGO (Baryon Acoustic Oscillations in Neutral Gas Observations) has operational frequency from 960 MHz to 1260 MHz (Battye et al. 2013; Wuensche & the BINGO Collaboration 2019) and MeerKAT's frequency bandwidth ranges from 900-1185 MHz and 580-1000 MHz for L-band and UHF-band, respectively (Wang et al. 2021; Cunnington et al. 2022).

We show examples for the first time of calculations of the auto- and cross-power for HI and convergence in Fig. 1 using Eq. 8. As expected, the auto- signal depends on the radial HI width σ_χ , while the cross-power is insensitive to this.

2.2 Lensing Convergence and HI Intensity Maps

The full-sky gravitational lensing mock catalogues by Takahashi et al. (2017) have been used throughout this work. They are based on a multiple-lens ray-tracing approach through N-body cosmological simulations. The datasets include weak lensing maps (convergence, shear and rotation data) up to redshift 5.3, and halo catalogues. The catalogues provide 108 realisations of N-body simulations, 35 of which are used in this research (due to storage limitations). The N-body simulations were produced with periodic boundary conditions following dark matter gravitational evolution without baryonic processes. 14 simulation boxes of side length $L = 450$,

900, 1350, ..., 6300 $h^{-1}\text{Mpc}$ are nested to represent a region of the Universe in which lensing occurs; each box contains 2048^3 particles. The κ fields are obtained by tracing the light ray path through planes with separation $150 h^{-1}\text{Mpc}$. By calculating the Jacobian matrix A along the light path, the lensing convergence κ , shear lensing $\gamma_{1,2}$ and rotation angle ω can be obtained, via

$$A = \begin{bmatrix} 1 - \kappa - \gamma_1 & -\gamma_2 - \omega \\ -\gamma_2 + \omega & 1 - \kappa + \gamma_1 \end{bmatrix}. \quad (9)$$

The convergence maps were created in the HEALPIX scheme with NSIDE of 4096 (Górski et al. 2005), which contain 200 megapixels. While this resolution is appropriate to study nonlinear structure and matches forthcoming galaxy surveys such as EUCLID¹ and DESI², the cross-correlation between the lensing convergence and the HI intensity map is limited by the lower angular resolution of HI intensity maps expected with real radio telescopes. Therefore the resolution is reduced to NSIDE of 512; this is not only appropriate for our 2-point function measurements but also decreases the storage space requirement and computational time.

We will first consider a convergence map at a specific optical lensing catalogue source redshift, which we choose as $z \approx 0.78$, for which the lensing will significantly occur at the redshift of an intensity map at redshift ≈ 0.3 . This particular choice of redshift allows us to compare our results to current and forthcoming optical and radial surveys (Baxter et al. 2019; Square Kilometre Array Cosmology Science Working Group et al. 2020; Euclid Collaboration 2019; Pourtsidou et al. 2017; Santos et al. 2015). We will then extend to multiple lensing planes (see Table 1).

We turn now to generating our IM maps. Crucially, we will emulate removal of the IM foreground by removing the radial temperature fluctuations on large scales. The foreground removal will be discussed in detail in Section 3.

First we need to make the pre-foreground-removal IM maps. Instead of calculating the individual HI masses M_{HI} from halo catalogues, we assume that HI is a biased tracer of the total matter overdensity field $\delta(\theta, z)$ (see Eq. 4 and 5),

$$\delta_{\text{HI}}(\hat{n}, z) \equiv \frac{T_{\text{HI}}(\hat{n}, z) - \bar{T}_{\text{HI}}(z)}{\bar{T}_{\text{HI}}(z)} = b_{\text{HI}}(z)\delta(\hat{n}, z), \quad (10)$$

where b_{HI} is a HI bias. For instance the parametric form for b_{HI} adopted by Cunnington et al. (2019b) is

$$b_{\text{HI}}(z) = 0.67 + 0.18z + 0.05z^2. \quad (11)$$

Since the neutral hydrogen signal is measured as the surface brightness temperature, we shall refer to the HI intensity map as the temperature fluctuation ΔT_{HI} :

$$\Delta T_{\text{HI}}(\hat{n}, z) = T_{\text{HI}}(\hat{n}, z) - \bar{T}_{\text{HI}}(z) = \bar{T}_{\text{HI}}(z)b_{\text{HI}}(z)\delta(\hat{n}, z). \quad (12)$$

We apply this equation to the overdensity map obtained from Takahashi et al. (2017) catalogues to create HI intensity maps. Fig. 2 shows the uncleaned and cleaned intensity maps from one realisation for the zoom-in patch with area 5×5 square degrees.

As we are interested in the 2-dimensional projection of cosmological fields on the sky, together with their power spectra, it is convenient to describe these fields $\Theta(\hat{n}, z)$ in spherical harmonics:

$$\Theta(\hat{n}, z) = \sum_{\ell=0}^{\infty} \sum_{m=-\ell}^{m=\ell} a_{\ell m}(z) Y_{\ell}^m(\hat{n}), \quad (13)$$

¹ <https://www.euclid-ec.org/>

² <https://www.desi.lbl.gov/>

where $Y_\ell^m(\hat{n})$ and $a_{\ell m}(z)$ are spherical harmonics and their coefficients respectively (Pratten et al. 2016; Castro et al. 2005; Heavens 2003). $\Theta(\hat{n}, z)$ represents an arbitrary cosmological field; in this work it can be either lensing convergence or HI temperature fluctuations. The angular power spectrum is then an average of $a_{\ell m}$ over m modes:

$$C^{XY}(\ell) = \langle a_{\ell m}^X(z_1) a_{\ell m}^{Y*}(z_2) \rangle, \quad (14)$$

where X and Y stand for the cosmological fields at given redshifts z_1 and z_2 , respectively.

The cross power-spectrum for HI and lensing κ can be easily measured via HEALPIX's *anafast* routine especially if the data is for the full sky (however, if the data has missing regions or a cut sky, pseudo- C_ℓ methods are required (Brown et al. 2005; Upham et al. 2019)).

Using this routine, we obtain cross-power measurements for the HI and κ fields. We measure the cross-power spectra of 35 realisations and evaluate their mean; we show the results in Fig. 3. Here the lensing convergence is measured at the central redshift 0.78 and HI is measured at the central redshift 0.3. Fig. 3 also displays a comparison between theoretical 2-point statistics and the measurements from the mock catalogues. We then measure the covariance matrices $\mathbf{COV}(C^{XY})$ of 2-point statistics from 35 realisations. The error bars are the square root of the diagonal elements of $\mathbf{COV}(C^{XY})$ of the estimators. The correlation matrix for $\mathbf{COV}(C^{XY})$ are shown in Fig. 6.

We see that the measurements from simulations agree very well with our theory curves on this plot, which indicates that our theoretical calculation and selection function $n_{\text{HI}}^i(z(\chi))/\bar{n}_{\text{HI}}^i$ successfully match the simulations. Due to the lens shell approximation of the ray tracing code, the measured C_ℓ is slightly affected at very high ℓ (see red line on Fig. 3).

3 HI FOREGROUND REMOVAL AND ITS EFFECT ON κ HI 2-POINT FUNCTIONS

The HI signal is small compared to its foregrounds such as free-free thermal emission, extragalactic radio sources and Galactic synchrotron. For example, the synchrotron (T_{sync}) emission temperature which can be modelled by $T_{\text{sync}} \propto (1+z)^{2.7}$ [K] (Platania et al. 1998; Smoot & Debono 2017), is approximately 3 to 4 orders of magnitude larger than T_{HI} at low redshift. Thus, 21cm foreground removal is a major challenge for HI cosmology. Several studies suggest that the foreground spectrum appears to be smooth in the radial direction (Cunnington et al. 2019a,b; Shaw et al. 2014). This is equivalent to being present in the long radial wavelengths in Fourier space. We therefore remove such modes in the line of sight background temperature fluctuations $\Delta T_{\text{HI}}^{\text{LoS}}(\hat{n})$.

Since the calculation of lensing involves integration along the light path (Eq. 3), which will have a contribution from long-wavelength radial modes, the HI foreground removal is a concern for the existence of the κ HI cross-correlation (i.e. we have just removed such modes from the HI signal). In this section we therefore seek to ascertain the degree to which the κ HI cross-correlation survives foreground removal.

Here we follow the method for foreground removal emulation by Cunnington et al. (2019b). The cleaned intensity map $\Delta T_{\text{HI}}^{\text{clean}}$ can be approximated as

$$\Delta T_{\text{HI}}^{\text{clean}}(\hat{n}, z) = \Delta T_{\text{HI}}^{\text{orig}}(\hat{n}, z) - \Delta T_{\text{HI}}^{\text{LoS}}(\hat{n}), \quad (15)$$

where $\Delta T_{\text{HI}}^{\text{orig}}(\hat{n}, z)$ is the uncleaned signal in direction \hat{n} at redshift

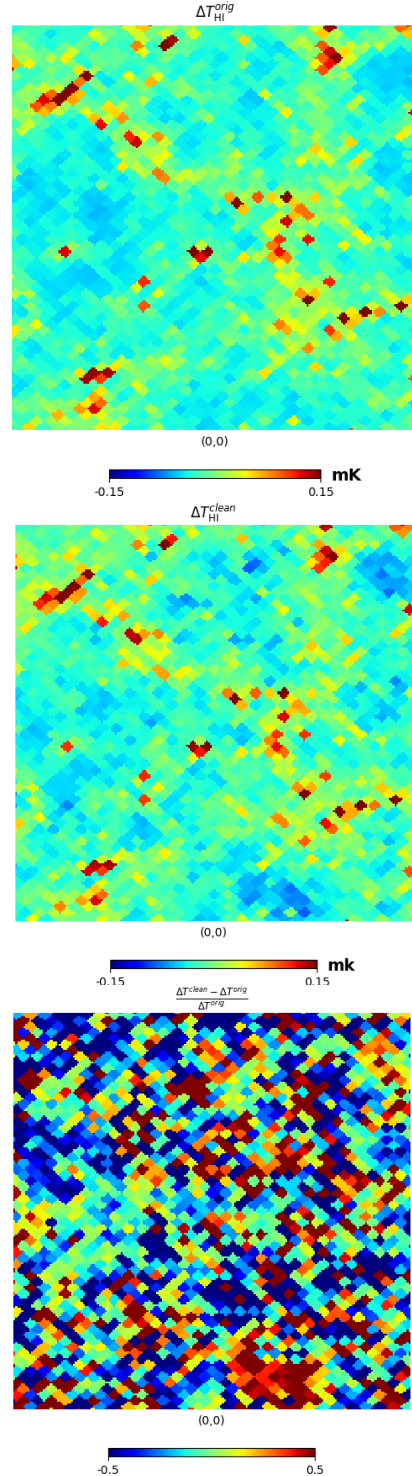


Figure 2. Top: the uncleaned intensity map, $\Delta T_{\text{HI}}^{\text{orig}}$, at $z = 0.3$ from an example realisation. The fluctuations were measured by assuming $b_{\text{HI}}(z)$ (see Eq. 12 and 17). Middle: the foreground-removed intensity map, $\Delta T_{\text{HI}}^{\text{clean}}$, at the same redshift. The foregrounds were removed by eliminating radial long wavelength modes up to redshift $z_{\text{max}} = 1$. The NSIDEs of the fluctuation maps is reduced from 4096 to 512 to match the resolution of forthcoming radio surveys. Bottom: residual map of cleaned and uncleaned maps. Each of these detail maps has area 5×5 square degrees (a small patch of the entire sky maps).

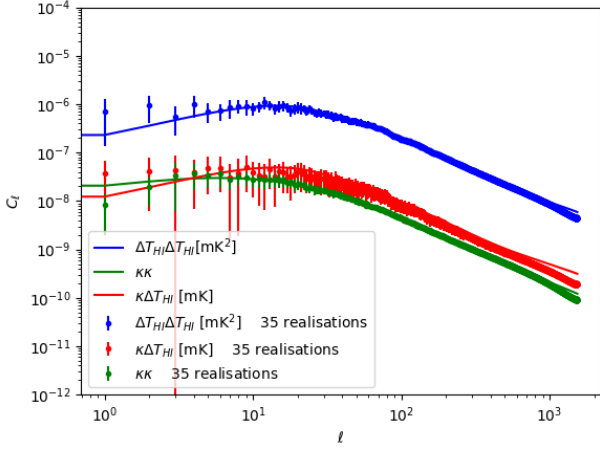


Figure 3. Comparison between theoretical C_ℓ (see Eq. 8) and measured C_ℓ from our simulations. Here the lensing convergence is measured at central redshift 0.78 and HI is measured at central redshift 0.3.

z . $\Delta T_{\text{HI}}^{\text{LoS}}(\hat{n})$ is defined by:

$$\Delta T_{\text{HI}}^{\text{LoS}}(\hat{n}) = \frac{1}{N_z} \sum_i \bar{T}_{\text{HI}}(z_i) b_{\text{HI}}(z_i) \delta(\hat{n}, z_i), \quad (16)$$

so that $\Delta T_{\text{HI}}^{\text{LoS}}(\hat{n})$ is the mean surface brightness temperature fluctuation along the entire line of sight. This is an initial very approximate model of Principal Component Analysis (PCA) foreground removal, as most dominant components are included in the line of sight expectation temperature fluctuations $\Delta T_{\text{HI}}^{\text{LoS}}(\hat{n})$. It is worth mentioning that this blind foreground removal technique assumes the smoothness of the foreground. However, this smoothness can be hampered by non-smooth features of the beam, e.g. beamwidth of the radio dish, and some oscillating features in all bands of MeerKAT. A simple $1/f$ dependence of the beam could generate artificial HI signals. This leads to the conclusion in Spinelli et al. (2022) that it is fundamental to develop accurate beam deconvolution algorithms and test data post-processing steps carefully before cleaning. This topic of beam deconvolution is beyond the scope of our research; here we shall assume that the $1/f$ behaviour is sufficiently small. For more sophisticated foreground cleaning methods we encourage the reader to explore e.g. Cunnington et al. (2023).

In this work we adopt the same bias model as Cunnington et al. (2019a):

$$b_{\text{HI}}(z) = \alpha(b_0 + b_1 z + b_2 z^2), \quad (17)$$

where α , b_0 , b_1 and b_2 are set to 1, 0.67, 0.18 and 0.05, respectively. Cunnington et al. (2019a) obtained this parameter set by investigating HI as a biased tracer of the large-scale structure via HI intensity map and optical galaxy number density cross-correlations (see Eq. 39 from Cunnington et al. (2019a)). We use this as a fiducial model since the HI redshift range in our work is similar to Cunnington et al. (2019b,a). Note that in this model, we solely account for the redshift evolution of HI bias and assume any transverse scale dependence of the bias is negligible. Martin et al. (2012) shows that this is a good approximation for scales $> 10 h^{-1} \text{Mpc}$, which are our main interest.

We measure $\Delta T_{\text{HI}}^{\text{LoS}}$ with two choices of maximum redshift, $z_{\text{max}} = 1$ and 3. $z_{\text{max}} = 3$ corresponds to futuristic HI-galaxy surveys (Square Kilometre Array Cosmology Science Working Group

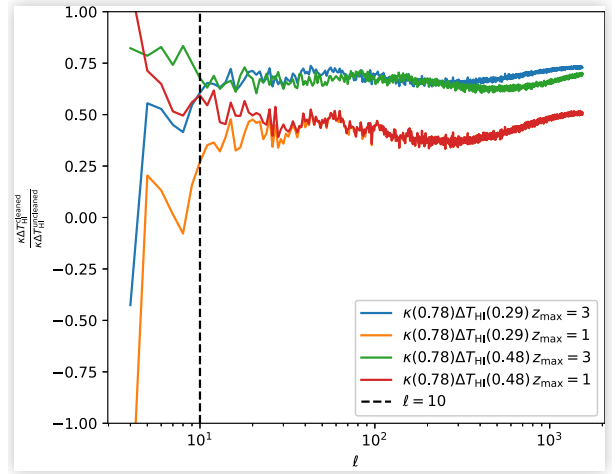


Figure 4. The ratio between cleaned and uncleaned $\kappa \Delta T_{\text{HI}}$ power spectra. Two maximum redshifts (z_{max}) for foreground removal are considered; $z_{\text{max}} = 1$ corresponds to current and imminent radio dishes meanwhile $z_{\text{max}} = 3$ represents a future SKA survey.

et al. 2020). On the other hand $z_{\text{max}} = 1$ is an approximate limit for HI maps with SKA1-MID and MeerKAT (Square Kilometre Array Cosmology Science Working Group et al. 2020; Cunnington et al. 2022).

We use these intensity maps with removed foreground to calculate the auto-power spectra of the intensity map ($\Delta T_{\text{HI}} \Delta T_{\text{HI}}$), and the cross-power spectra between HI and κ ($\kappa \Delta T_{\text{HI}}$). We compare the signal of removed and unremoved $\kappa \Delta T_{\text{HI}}$, resulting in Fig. 4 and Fig. 5. From Fig. 4, we note that foreground removal strongly affects the signal on large scales. However we find that on smaller scales, at $\ell > 10$, the foreground removal does not erase the $\kappa \Delta T_{\text{HI}}$ power spectrum; the signal is scaled down by a factor (A_{clean}) which is close to constant over a range of ℓ modes from 10 to 1000. Hence, in section 4, when cosmological constraints following foreground removal are considered, the estimation of cosmological parameters is based on the signal where $\ell > 10$. We describe the mean signal drop A_{clean} by:

$$A_{\text{clean}}(z_{\text{HI}}, z_{\kappa}, z_{\text{max}}) \equiv \left\langle \frac{\kappa \Delta T_{\text{HI}}^{\text{uncleaned}}}{\kappa \Delta T_{\text{HI}}^{\text{cleaned}}} \right\rangle_{10 < \ell < 1500}. \quad (18)$$

From Fig. 4, we see that the higher the maximum redshift of the survey in which we remove the LOS signal, the less is the effect on the cleaned cross-correlation signal, as more radial modes are preserved in the removal process. Fig. 4 and 5 further indicate that the signal in the κ HI 2-point correlations drops by approximately the same factor A_{clean} across a wide redshift range, if we remove the background noise up to a particular redshift z_{max} , when cross-correlating to the κ field at a fixed redshift. Fig. 5 also implies that $A_{\text{clean}}(z_{\text{HI}}, z_{\kappa}, z_{\text{max}1}) < A_{\text{clean}}(z_{\text{HI}}, z_{\kappa}, z_{\text{max}2})$ if the maximum redshifts $z_{\text{max}1} > z_{\text{max}2}$.

4 FISHER FORECAST

In previous sections, we have presented the theoretical 2-point statistics for the HI-lensing cross-correlation, and have examined the impact of HI foreground removal on the cross-power spectrum. The results indicate that foreground removal reduces the 2-point statistics by a modest factor.

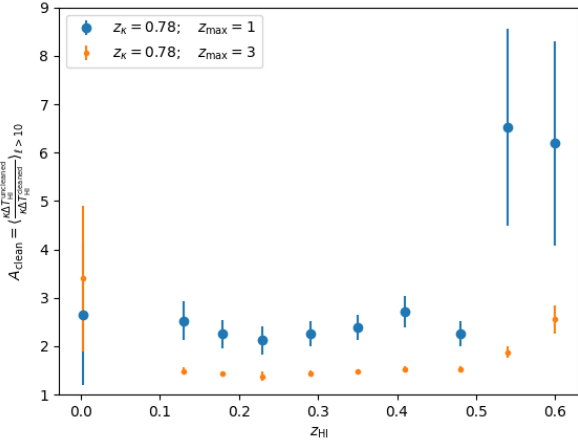


Figure 5. The average ratio A_{clean} over $\ell > 10$ modes, as a function of redshift of HI slice used in the cross-correlation.

Here we begin the exploration of κ HI correlations as a tool for cosmological constraints. In particular we will make a Fisher information matrix forecast of this correlation in the case of low instrumental noise (but including our foreground subtraction model); this will assess the best-case capacity of this probe to constrain cosmology, when one is dominated by large-scale structure fluctuations in the HI and lensing fields. We will then examine more realistic cases with cut sky and the inclusion of instrumental noise.

4.1 The Fisher matrix

The Fisher information matrix is a useful tool to estimate the expected uncertainty in cosmological parameters for forthcoming experiments (Heavens 2003; Tegmark et al. 1997). Assuming that the model parameters θ_i are distributed by a multivariate Gaussian likelihood L , the Fisher matrix can be calculated as

$$F_{ij} \equiv \left\langle \frac{\partial^2 \mathcal{L}}{\partial \theta_i \partial \theta_j} \right\rangle, \quad (19)$$

where $\mathcal{L} = -\ln L$. The Fisher matrix can be used to obtain the minimum uncertainty (σ_i) in parameter estimation due to the Cram er-Rao inequality (Mendez et al. 2014; Kamionkowski et al. 2011),

$$\sigma_i \geq \sqrt{F_{ii}^{-1}}, \quad (20)$$

which is equivalent to a 68% confidence level. For a dataset where the uncertainties are Gaussian, the Fisher matrix can be calculated by (Tegmark et al. 1997)

$$F_{ij} = \frac{1}{2} \text{Tr}[A_i A_j + C^{-1} M_{ij}] \quad (21)$$

where C denotes the covariance matrix of the data, $A_i \equiv C^{-1} C_{,i}$, the derivative data matrix $M_{ij} \equiv \mu_{,i} \mu_{,j}^T + \mu_{,j} \mu_{,i}^T$, and μ is an expectation value of the data vector x . The comma symbol means the partial derivative operator with respect to the parameter, $\mu_{,i} \equiv \partial \mu / \partial \theta_i$. Note that all derivatives are performed at the maximum likelihood point.

As we expect only small changes in the covariance matrix $\text{COV}(C^{XY})$ under a modest change in cosmological parameters

(see Sec. 2 and 3), the first term on the right hand side in Eq. 21 will be negligible. Then the Fisher matrix can be written

$$F_{ij} = \sum_{XY} \frac{\partial C^{XY}}{\partial \theta_i} \text{COV}(C^{XY})^{-1} \frac{\partial C^{XY}}{\partial \theta_j}. \quad (22)$$

We calculate the cross-power spectra $C^{XY}(\ell)$ by using Eq. 8 with Planck 2018 cosmological parameters (Planck Collaboration et al. 2018). We calculate the covariance matrices of $\kappa\kappa$, κ HI and HIHI from measured cross-power-spectra of 35 realisations of the N-body simulation by Takahashi et al. (2017). All the HI temperature fluctuation maps which we use take into account foreground removal. We also calculate the correlation matrices $\text{CORR}_{ij} = \text{COV}_{ij} / \sqrt{\text{COV}_{ii} \text{COV}_{jj}}$ and show these in Fig. 6; these do not indicate significant correlations between ℓ bins.

4.2 Cosmological Constraints for Single-Slice Cross-correlations

In this section, the cosmological constraint viability of κ and HI cross-correlations is explored. We first start with the simplest observational configuration, considering only one redshift slice of HI and κ . We further assume that the $b_{\text{HI}}(z)$ behaves as in Eq. 17. We use the Planck 2018 cosmological parameters as the fiducial cosmology (Planck Collaboration et al. 2018). The fiducial cosmological parameters are $h = 0.67$, $\Omega_m = 0.3$, $\sigma_8 = 0.82$, $\Omega_k = 0$, $\Omega_\Lambda = 0.7$, $\tau = 0.06$, and $n_s = 0.96$. To make a covariance matrix of cross-power spectra for the Fisher matrix (Eq. 22), we combine ℓ modes into 15 bins; each bin contains 101 ℓ modes with $11 \leq \ell \leq 1527$ and averages over 35 realisations. We first consider the 3×2 functions for a joint analysis of $\kappa(0.78)\kappa(0.78)$, $\Delta T_{\text{HI}}(0.3)\Delta T_{\text{HI}}(0.3)$ and $\kappa(0.78)\Delta T_{\text{HI}}(0.3)$, where the numbers in brackets are the central redshifts. We choose these central redshifts as examples of current HI and lensing surveys' central redshifts. The '2x2' functions refer to the same combination but exclude the weak lensing-HI cross power spectrum.

Fig. 7 shows the joint likelihood obtained via Fisher matrices (see Eq. 22). We see that single redshift slice correlations of $\kappa - \kappa$ (green) and HI-HI (grey) provide relatively weak constraints, while 2x2pt and particularly 3x2pt are more promising, with few-to ten-per cent constraints available on parameters in this low noise case. The zoom-in version of 3×2 pt functions is shown on the right hand side of Fig. 7; these likelihood contours, which include the cross-correlation, show a significant improvement in cosmological constraints compared to $\kappa\kappa$ or $\Delta T_{\text{HI}}\Delta T_{\text{HI}}$ constraints alone. Therefore in the next section, we will examine a joint likelihood between more redshift bins, and where the HI bias ($b_{\text{HI}}(z)$) is taken into account.

4.3 HI bias and multi-redshift bin joint likelihood analysis

It is well known that there is a degeneracy between galaxy bias, Ω_m and σ_8 in parameter constraints, since these parameters all affect the amplitude of the power spectrum (see Eq. 8). However, they contribute differently to the evolution of the power spectrum with time; hence by measuring the power spectra in various redshifts we can break the degeneracies between them. From Eq. 8, we can see that while $\Delta T_{\text{HI}}\Delta T_{\text{HI}}$ measures $b_{\text{HI}}^2(z)$, $\kappa\Delta T_{\text{HI}}$ additionally measures $b_{\text{HI}}(z)$. Combining the cross-bin intensity mapping power spectra with the $\kappa\Delta T_{\text{HI}}$ cross-spectra we can therefore tighten our constraints on bias and cosmological parameters.

In this section we consider two different bias models, with

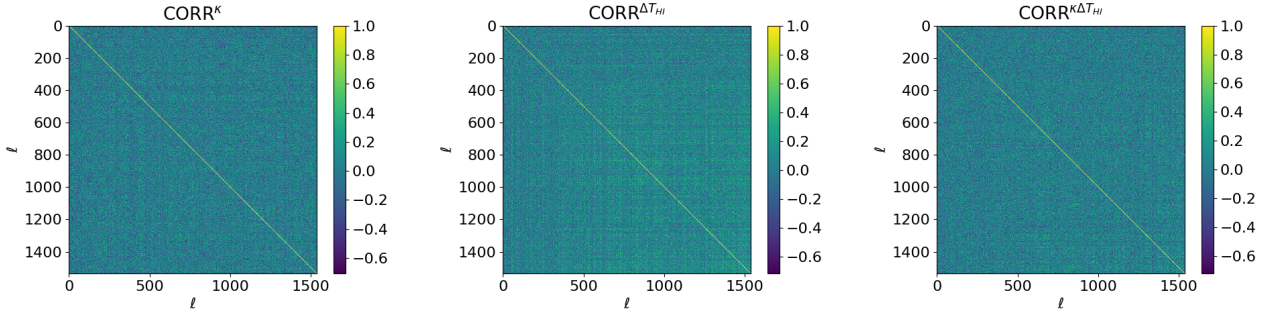


Figure 6. The correlation matrices of C_ℓ^{XY} measured from 35 realisations for the cleaned HI signal at central redshift $z = 0.3$ and κ signal at $z = 0.78$. Left: $\kappa\kappa$, middle: $\Delta T_{\text{HI}}\Delta T_{\text{HI}}$ and right: $\kappa\Delta T_{\text{HI}}$.

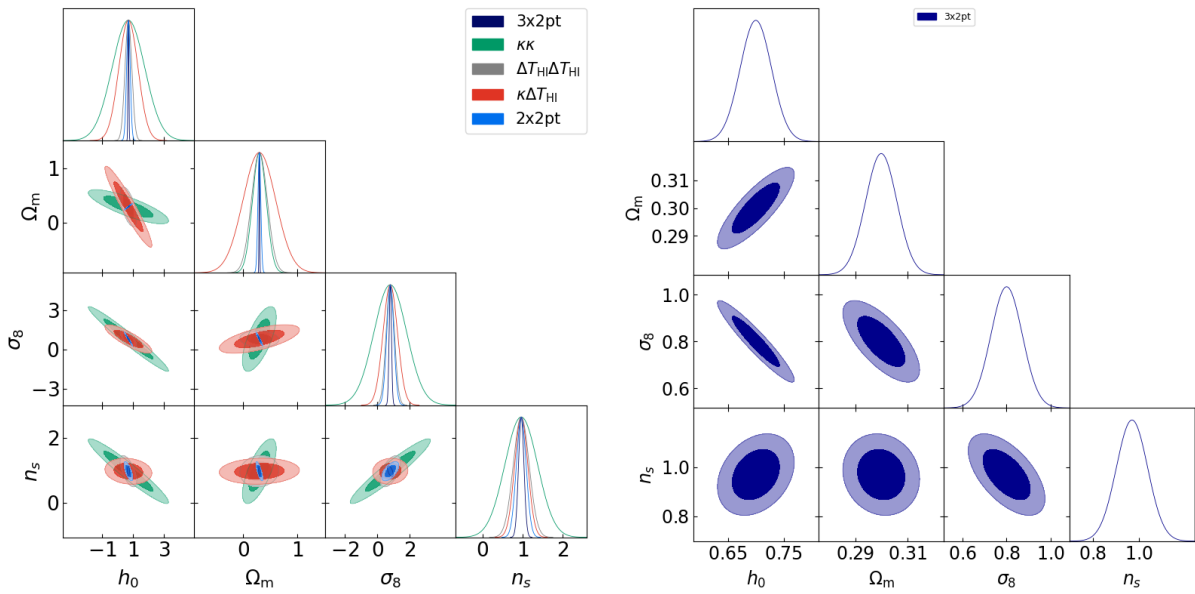


Figure 7. Left: Likelihood contours for the dataset described in section 4.2; contours show 68% and 95% confidence levels. Right: zoom-in of likelihood contours of 3x2-point functions and their marginalisations from the left panel.

distinct parameter sets. The first, more restricted model explores bias amplitude variation via the α parameter in Eq. 17, setting the rest of the parameters to the best fit values (Cunnington et al. 2019b). In the second model, b_0, b_1 and b_2 are the bias parameters with α set to equal 1. We include these parameters when evaluating the Fisher matrices (Eq. 22). Note that both b_{HI} models are scale-invariant and depend only on z . We will consider both full-sky and 300 deg² surveys to explore the viability of HIHI and κ HI in cosmological constraints.

For the full-sky case, as we include more parameters for b_{HI} , we also examine more redshift bins for both HI and κ to obtain the best possible results. We consider the redshift range for ΔT_{HI} which would be measured by pre-SKA and SKA-MID experiments (Square Kilometre Array Cosmology Science Working Group et al. 2020; Poursidou et al. 2017; Santos et al. 2015). Table 1 shows the central redshifts we consider for ΔT_{HI} and κ bins; the width of each bin is $150 h^{-1} \text{Mpc}$, $\Delta z \approx 0.05$. Table 1 lists both HI and κ central redshifts. As we have 16 z_{HI} , we shall refer to '16-HIHI' which corresponds to 16 pairs of HI auto-correlation functions; we cross-correlate HI intensity maps to κ fields at $z_\kappa = 0.44, 0.78$ and 1.77 respectively. We refer to 16-HIHI+1- κ as the

joint analysis for 16-HIHI and κ HI 2-point statistics at which $z_\kappa = 0.44$. We add further z_κ bins and label joint data as 16-HIHI+2- κ and 16-HIHI+3- κ . We calculate both the futuristic case where HI can be measured with high $\ell_{\text{max}} \geq 1000$ and the current state of art where $100 < \ell_{\text{max}} < 400$.

We further calculate the figure of merit (FoM) for the $\Omega_m - \sigma_8$ constraint. The FoM is the inverse of the area of the $\Omega_m - \sigma_8$ contours; in this case we calculate the FoM at 95% confidence level. Fig. 8 shows the FoM of the $\Omega_m - \sigma_8$ constraints. The blue dots show the FoM from 16HIHI, where we consecutively add HI auto-correlations for the redshift bins in the order listed in Table 1. We see that all redshift bins contribute to an improved signal, with a nearly linearly increasing contribution (for this experiment, we are assuming that only $z < 1$ HI slices are available). The green, red and black dots in Fig. 8 show the FoM for $\ell_{\text{max}} = 1530$ when we further add the cross-correlations between consecutive HI slices and the κ slices at $z = 0.44, 0.78$ and 1.78 , respectively. We see that these cross-correlations significantly improve the FoM, and appear to be converging to a maximal constraint when including all slices.

We now present Fisher forecast results for the first bias model, using the redshift bins in Table 1. Fig. 10 shows the utility of multi-

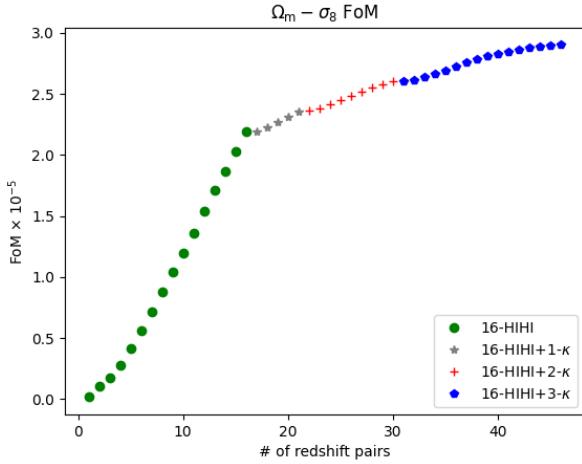


Figure 8. Figure of Merit for $\sigma_8 - \Omega_m$ constraints; the horizontal axis is the number of redshift bin pairs for cosmological constraints. We show cumulative FoM when including increasing numbers of HI auto-correlation redshift bins (green); then increasing numbers of cross-correlations with convergence bins (grey, red, blue). Here $\ell_{\max} = 1530$.

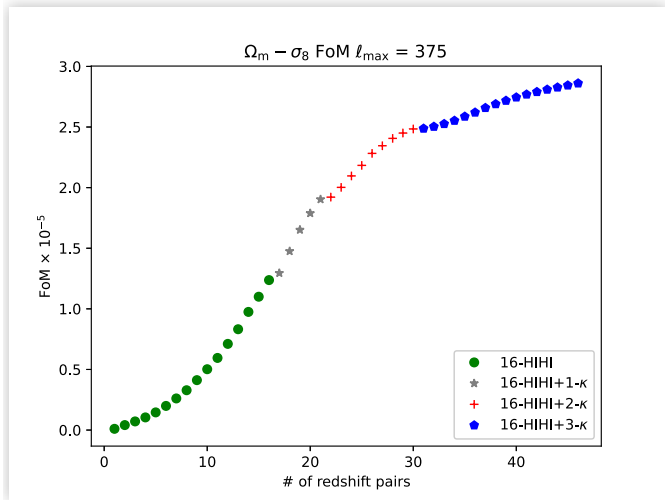


Figure 9. Figure of Merit for $\sigma_8 - \Omega_m$ constraints; the horizontal axis is the number of redshift bin pairs for cosmological constraints. We show cumulative FoM when including increasing numbers of HI auto-correlation redshift bins (green); then increasing numbers of cross-correlations with convergence bins (grey, red, blue). Here $\ell_{\max} = 375$.

redshift bin power spectra measurements with HI and κ . With the appropriate redshift bin size of HI (Δz_{HI}) for $\ell_{\max} = 1530$, we can achieve tight cosmological constraints (in this low noise case) which are comparable to the optical and CMB probes such as (Abbott et al. 2019; Alam et al. 2017; Planck Collaboration et al. 2018; Abbott et al. 2018). By including more κ redshift slices, the constraints are improved significantly especially for Ω_m and α . However, this also makes the contours more elliptical, as there are remaining degeneracies among parameters. The uncertainties on parameters are measured at 95% confidence level and reported in Table 2.

We next consider the current state of the art case, where since the typical angular resolution $\sim 1^\circ$, we set $\ell_{\max} = 375$ (we choose this particular value as it is convenient to consider the $\Delta\ell$ bins as 15

Table 1. The central redshifts for intensity and lensing convergence maps in our multi-redshift bin analysis. For $\kappa\Delta T_{\text{HI}}$, we require that $z_{\text{HI}} < 0.7z_\kappa$.

z_{HI}	z_κ
0.02	0.44
0.08	0.78
0.13	1.77
0.18	
0.24	
0.29	
0.35	
0.41	
0.47	
0.54	
0.60	
0.68	
0.75	
0.83	
0.91	
0.99	

Table 2. Cosmological forecast from Fisher analysis for 16-HIHI + 3- κ correlations; the uncertainties on cosmological parameters and HI bias are quoted at 95% confidence level. HI bias model 1 considers only the re-scaling parameter α . In contrast the second model considers quadratic parameters; b_2 is poorly constrained, while all other parameters are able to be measured well (see Fig. 12).

Parameters	HI bias model 1	HI bias model 2
Δh_0	± 0.02	± 0.02
$\Delta \Omega_m$	± 0.01	± 0.02
$\Delta \sigma_8$	± 0.03	± 0.04
Δn_s	± 0.04	± 0.05
$\Delta \alpha$	± 0.04	-
Δb_0	-	± 0.04
Δb_1	-	± 0.03

bins with $\Delta\ell = 25$). Fig. 9 shows the cumulative Figure of Merit in this case, while Fig. 11 illustrates the likelihood contours for cosmological parameters with this maximum multipole. Comparing with Fig. 10, where $\ell_{\max} = 1530$ we can see that there is a substantial difference in the 16-HIHI contours. However, we notice the significant improvement in parameter constraints when we add 3 κ bins to 16-HIHI (green shade) in $\ell_{\max} = 375$. We are therefore seeing that by joining κ HI 2-point statistics to HIHI auto-correlations, we can improve cosmological constraints significantly.

For bias model 2, we find that the second order coefficient of HI bias b_2 is very poorly constrained. Marginalising over this parameter does not significantly affect the other cosmological parameter constraints (h_0 , Ω_m , σ_8 and n_s). We set this parameter to 0.05 following Cunningham et al. (2019b). Fig. 12 shows the likelihood constraints for this model. We can see that by adding more κ slices, the h_0 constraints do not improve much but the improvement in the $\Omega_m - \sigma_8$ constraint can be easily noticed. The uncertainties on our HI bias models and cosmological parameters are reported in Table 2. Comparing the parameter constraints from both b_{HI} models (see Table 2), we notice that model 1 gives slightly better (but very comparable) cosmological constraints.

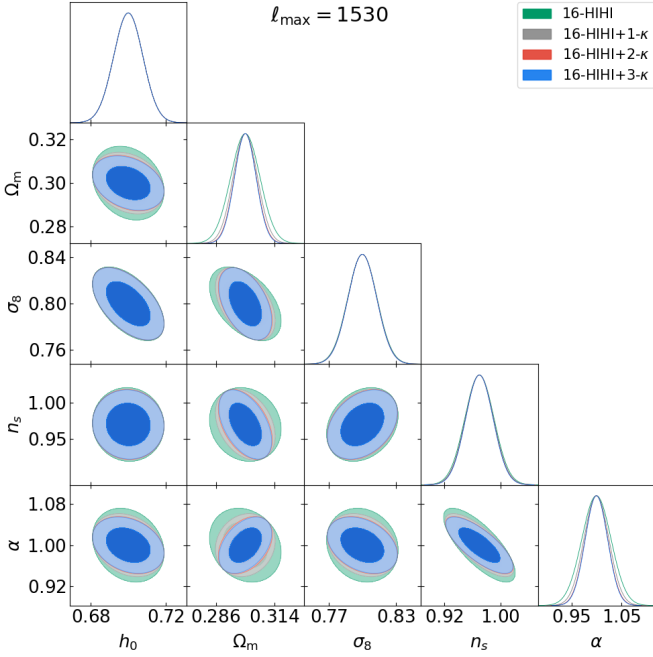


Figure 10. The likelihood contours for our multi-bin analysis with HI bias model 1 with $\ell_{\max} = 1530$; the contours show 68% and 95% confidence levels. The cosmological parameter uncertainties at 95% are measured and reported in Table 2.

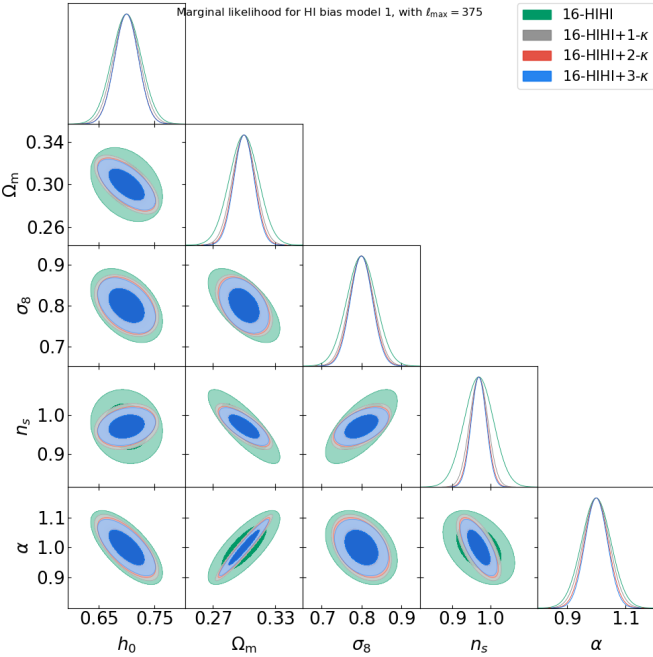


Figure 11. The likelihood contours for our multi-bin analysis with HI bias model 1 with $\ell_{\max} = 375$; the contours show 68% and 95% confidence levels. Compared to Fig. 10, we can see the difference in 16-HIHI constraint. However, when combining the κ HI-correlation the constraints are similar to those in Fig. 10.

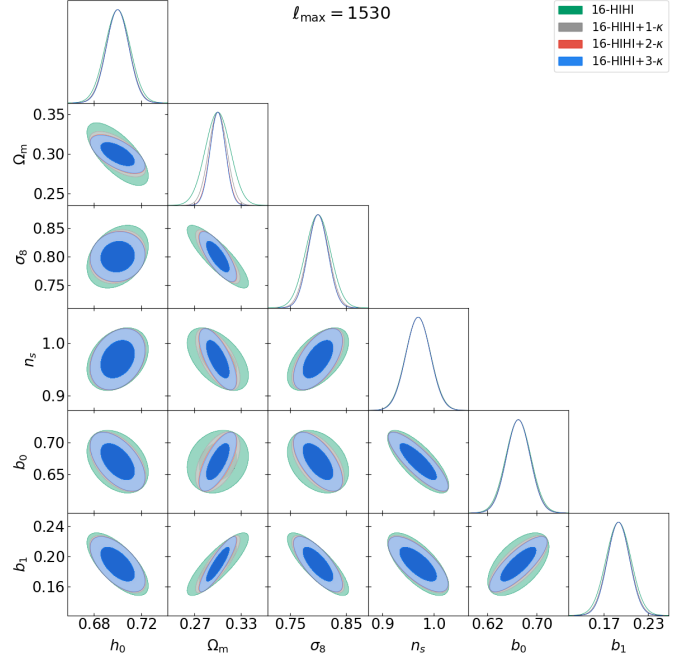


Figure 12. Constraints on cosmological parameters and $b_{\text{HI}}(z)$ for our second bias model, for 2-point functions at 68% and 95% levels of confidence (for our 16HIHI redshift slice case). The κ HI correlation functions do not significantly improve the h_0 , n_s , b_0 and b_1 constraints. For this figure, we marginalised over b_2 as it is poorly constrained. However, we see significant improvement in Ω_m and σ_8 constraints. The parameter uncertainties at 95% level are reported in Table 2.

4.4 The effect of sky coverage

Now let us consider the effect of sky coverage area on 2-point statistics of both HIHI auto and κ HI cross angular power spectra. We now consider a combined survey area 300 deg^2 of lensing and HI observations, comparable to current pathfinder intensity mapping surveys. As this area is much smaller than the full-sky case, we therefore now need to use the pseudo angular power (\tilde{C}_ℓ) as an estimator of C_ℓ .

Suppose the survey footprint of the observations can be expressed using the weight function $W(\hat{n})$. Normalised by the sky factor f_{sky} (the fraction of the sky covered by the data), the weight moments are given by:

$$f_{\text{sky}} w_i = \frac{1}{4\pi} \int d\hat{n} W^i(\hat{n}), \quad (23)$$

where w_i represents the i -th moment of weighting. The power spectrum of the window function is:

$$\mathcal{W}_\ell = \frac{1}{2\ell + 1} \sum_m |w_{\ell m}|^2. \quad (24)$$

For a spin-0 field $\zeta(\hat{n})$ weighted by $W(\hat{n})$, a spherical harmonic coefficient $\tilde{a}_{\ell m}$ can be expressed as (Kim & Naselsky 2010; Kim 2011):

$$\tilde{a}_{\ell m} = \int d\hat{n} \zeta(\hat{n}) W(\hat{n}) Y_{\ell m}^*(\hat{n}) \approx \Omega_p \sum_p \zeta(p) W(p) Y_{\ell m}^*(p), \quad (25)$$

where we approximate the integration over sky factor by the summation over pixel area with the surface density Ω_p . The pseudo

power spectrum estimator, \tilde{C}_ℓ , is then:

$$\tilde{C}_\ell = \frac{1}{2\ell+1} \sum_m |\tilde{a}_{\ell m}|^2. \quad (26)$$

Similarly for spin-2 fields (γ_1, γ_2), we can obtain the coefficients, $\tilde{a}_{\pm 2, \ell m}$, by:

$$\tilde{a}_{\pm 2, \ell m} = \int [\tilde{\gamma}_1(\hat{n}) \pm i\tilde{\gamma}_2(\hat{n})]_{\pm 2} Y_{\ell m}^*(\hat{n}) d\hat{n}, \quad (27)$$

where

$$\tilde{\gamma}_1(\hat{n}) \pm i\tilde{\gamma}_2 = W(\hat{n})[\gamma_1(\hat{n}) \pm i\gamma_2(\hat{n})]. \quad (28)$$

Similarly to the full-sky case, $\tilde{a}_{\ell m}^E$ and $\tilde{a}_{\ell m}^B$ are then:

$$\tilde{a}^E = -(\tilde{a}_{2, \ell m} + \tilde{a}_{-2, \ell m})/2, \quad (29)$$

$$\tilde{a}^B = i(\tilde{a}_{2, \ell m} - \tilde{a}_{-2, \ell m})/2. \quad (30)$$

The pseudo power spectra for E and B modes are:

$$\tilde{C}_\ell^{E,B} = \frac{1}{2\ell+1} \sum_m |\tilde{a}_{\ell m}^{E,B}|^2. \quad (31)$$

The pseudo power spectra \tilde{C}_ℓ and true C_ℓ are related by the mode-mode coupling resulting from masking ($M_{\ell\ell'}$):

$$\langle \tilde{C}_\ell \rangle = \sum_{\ell'} M_{\ell\ell'} \langle C_{\ell'} \rangle. \quad (32)$$

This kernel depends solely on the geometry of a cut-sky \mathcal{W}_ℓ and plays a crucial role in the pseudo- C_ℓ method. For details concerning the mode-mode coupling, see [Hivon et al. \(2002\)](#); [Alonso et al. \(2019\)](#).

We utilise NaMaster ([Alonso et al. 2019](#)), which is a software package to calculate pseudo- C_ℓ for any spin fields, to evaluate HIHI and κ HI pseudo- C_ℓ for 300 deg² of our simulations above, within a masked region RA = [0, 30] deg and dec = +[0, 10] deg, for the same redshift bins (see Table 1). We choose the same ℓ bins as before up to $\ell < 375$ with $\theta_{\text{beam}} = 1$ deg convolution, and calculate the cut-sky covariance matrix using NaMaster. Fig. 13 shows the cosmological constraints feasible of this scenario. Comparing the results to the full-sky case (Fig. 11), we can see that the statistical incompleteness due to having a cut-sky survey reduces the feasibility; with 300 deg² sky, we cannot detect the HIHI cosmic signal. However, incorporating the cross-correlation with weak lensing improves the significance of the joint statistics (Fig. 13).

5 INSTRUMENT NOISE

In this section we consider the instrument noise for both lensing and HI surveys for the current state of art case. We will consider the expected thermal noise for a single-dish survey for HI measurement.

5.1 Single Dish Thermal Noise

We begin by examining the noise on 3D measured power spectra for the HI auto-correlation (P). This discussion is based on the works of ([Battye et al. 2013](#); [Santos et al. 2015](#); [Bigot-Sazy et al. 2015](#)). Subsequently, we derive the root mean square (rms) thermal noise expected on IM maps from the power spectra, which we will use to assess the effect of realistic noise on the ability to detect the lensing-HI cross-correlation.

The expected uncertainty (σ_P) on the power spectrum P can be

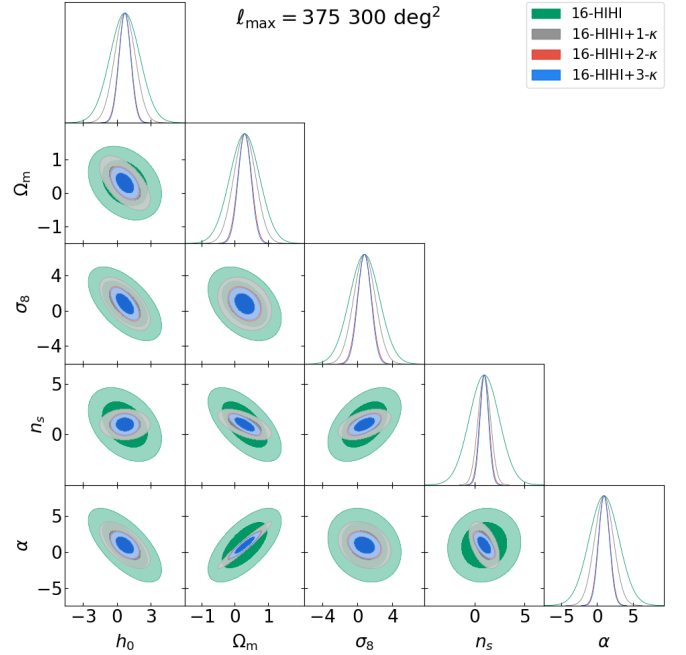


Figure 13. Constraints on cosmological parameters and $b_{\text{HI}}(z)$ for 2-point functions at 68% and 95% levels of confidence, for the small area 300 deg² case. This plot indicates that the feasibility of κ HI (pseudo) 2-point statistics in cosmological constraints is heavily affected by the statistical incompleteness due to having a small-sky survey.

estimated by evaluating its expected second moment. By calculating the ratio between σ_P and P averaging over the radial wavenumber bin size Δk , we can estimate the uncertainty in the IM map measurements. Following this procedure the error on P can be estimated by the following expression ([Seo et al. 2010](#); [Feldman et al. 1994](#); [Battye et al. 2013](#)):

$$\frac{\sigma_P}{P} = 2\sqrt{\left(\frac{2\pi}{3}\right) V_{\text{sur}} \frac{1}{4\pi k^2 \Delta k} \left(1 + \frac{\sigma_{\text{pix}}^2 V_{\text{pix}}}{[\bar{T}(z)]^2 W(k)^2 P}\right)}, \quad (33)$$

where V_{sur} is the volume of survey, $W(k)$ is windows function, $\bar{T}(z)$ is the average temperature at given redshift z and V_{pix} is the pixel volume. In this work we shall ignore the contribution of shot noise and only consider the contribution from pixel (thermal) noise σ_{pix} . These parameters are discussed in detail in the following paragraphs.

It is essential to pick the proper size of Δk to optimise the viability of a single dish. As we focus on the cosmic signal the acoustic scale should be an aim. That means we require $\Delta k/k_A < 1$, where k_A is the wavenumber of acoustic scale. The volume of the survey V_{sur} can be computed by

$$V_{\text{sur}} = \Omega_{\text{sur}} \int_{z_{\text{min}}}^{z_{\text{max}}} dz \frac{dV}{dz d\Omega}, \quad (34)$$

where

$$\frac{dV}{dz d\Omega} = \frac{cr^2(z)}{H_0 E(z)}, \quad (35)$$

where we assume a flat universe. The window function $W(k)$ is set by the instrument's specification. As we map the δ_{HI} from multiple redshift bins, we can ignore the contribution of radial directions in $W(k)$. However for the angular direction, this is not the case.

Importantly, the angular resolution of the radio beam will define the noise level. We can model $W(k)$ by:

$$W(k) = \exp \left[-\frac{1}{2} k^2 r^2(z) \frac{\theta_{\text{FWHM}}}{8 \ln(2)} \right], \quad (36)$$

where θ_{FWHM} is the full width half max of angular resolution. Realistically, θ_{FWHM} depends on frequency (ν). However, in this analysis we assume the variation of θ_{FWHM} is small and negligible.

The pixel volume, V_{pix} , can be determined by

$$V_{\text{pix}} = \Omega_{\text{pix}} \int_{z_c - \Delta z}^{z_c + \Delta z} dz \frac{dV}{dz d\Omega}, \quad (37)$$

where z_c is the central redshift and Δz corresponds to frequency width ($\Delta\nu$) and Ω_{pix} is the pixel solid angle.

In radio astronomy we normally measure the signal in terms of power. The antenna temperature then generates the thermal noise; the pixel noise σ_{pix} can be approximated by (Santos et al. 2015; Seo et al. 2010),

$$\sigma_{\text{pix}} \approx \frac{T_{\text{sys}}}{\varepsilon \sqrt{t_p 2 \Delta\nu}}, \quad (38)$$

where t_p represents the observation time per pointing, ε (approximately 1) signifies the efficiency of the telescope, meaning that almost no signal is lost when radio radiation is transmitted to the antenna. T_{sys} represents the system temperature, which includes

$$T_{\text{sys}} = T_{\text{rx}} + T_{\text{spl}} + T_{\text{CMB}} + T_{\text{gal}}, \quad (39)$$

where we ignore the contribution from the Earth's atmosphere. T_{spl} is the spill over from ground radiation (approximately 3K), $T_{\text{CMB}} \approx 2.73\text{K}$ and galactic temperature $T_{\text{gal}} \approx 25\text{K}$ (408 MHz/ ν)^{2.75K} (Square Kilometre Array Cosmology Science Working Group et al. 2020). The observing time per pointing t_p relates to the total observation by $t_p = t_{\text{tot}} (\theta_{\text{B}})^2 / \Omega_{\text{sur}}$, where θ_{B} is an angular pixel size.

As σ_{pix} is the rms thermal noise, by definition its square is the power per pixel volume (P_N / V_{pix}). Therefore, the 3D noise power spectrum (P_N) is then (Battye et al. 2013; Santos et al. 2015)

$$P_N = \sigma_{\text{pix}}^2 V_{\text{pix}} = r^2 y \frac{T_{\text{sys}}^2 \Omega_{\text{sur}}}{2 \varepsilon^2 t_{\text{tot}}}, \quad (40)$$

where

$$y = cH(z)^{-1} \frac{(1+z)^2}{v_{21}}. \quad (41)$$

If we have N_{d} dishes where each dish has N_{b} beams, we can take less time for each pointing area. The noise power spectrum is then reduced to

$$P_N(N_{\text{d}}, N_{\text{b}}) = \frac{r^2 y T_{\text{sys}}^2 \Omega_{\text{sur}}}{2 \varepsilon^2 t_{\text{tot}} N_{\text{b}} N_{\text{d}}}. \quad (42)$$

To determine the optimisation of a survey strategy, we can estimate the suitable θ_{FWHM} and Ω_{sur} that minimises $\delta k_{\text{A}} / k_{\text{A}}$ for acoustic scale k_{A} . This acoustic scale k_{A} can be estimated by following the work of Blake & Glazebrook (2003); Battye et al. (2013),

$$\frac{P(k)}{P_{\text{ref}}} = 1 + Ak \exp \left[-\left(\frac{k}{0.1 h \text{Mpc}^{-1}} \right)^{1.4} \right] \sin(2\pi k / k_{\text{A}}), \quad (43)$$

where A is the overall amplitude which can be marginalised. The subscript 'ref' refers to reference cosmological parameters.

We now calculate the thermal noise of a MeerKAT-like instrument $\sigma_{\text{pix}}^{\text{MK}} = \sigma_{\text{T}}$. In this case we consider a single dish telescope consisting of 64 dishes of 13.5m diameter, operating in UHF, L and

Table 3. MeerKAT pilot survey specifications (Wang et al. 2021)

$\Delta\nu$	0.2 MHz
$N_{\Delta\nu}$	[200,250]
T_{rx}	$7.5 \times 10^3 + 10^3 (\nu[\text{MHz}]/1000 - 0.75)^2$ [mK]
t_{tot}	10.5 hours
z	[0.3885, 0.4623]
N_{dish}	64
T_{sys}	16×10^3 mK
N_{pix}	87500
θ_{FWHM}	1.48 deg
Ω_{sur}	200 deg ²

S-band. The MeerKAT pilot survey by Wang et al. (2021) focuses on L-band from 856 to 1712 MHz with 4096 frequency channels. This pilot survey has 10.5 hours observation time with approximately ~ 200 deg² observation field (Wang et al. 2021; Cunnington et al. 2022). The summary statistics of this MeerKAT pilot survey are listed in Table 3. Wang et al. (2021) show that for integrated frequency channels, they can achieve thermal noise $\sigma_{\text{T}} \approx 2$ mK.

If we use Eq. (38) and (39) together with Table 3, the expected σ_{pix} for a single frequency channel of MeerKAT pilot survey is

$$\sigma_{\text{pix}}(\Delta\nu = 0.2; 10\text{hr}) \approx 15 \text{ mK}, \quad (44)$$

where we assume each dish has equal efficiency $\varepsilon = 1$ and consider only a single frequency channel $\Delta\nu = 0.2$ MHz. If we consider the whole frequency range like (Wang et al. 2021) the $\sigma_{\text{T}} \approx 2$ mK.

We now consider the case where the total observation time $t_{\text{tot}} = 1000$ hours and 250 frequency channels with $\Delta\nu = 0.2$ MHz.

5.2 S/N of κ HI

In section 5.1 we have estimated the rms thermal noise for MeerKAT-like surveys similar to the current state-of-the-art. In this section we explore the future case, where the observation time t_{tot} can take longer than MeerKAT's pilot survey, and we assume a full-sky survey to estimate the best possible S/N for weak lensing-intensity mapping (κ HI) 2-point statistics. The estimate $\sigma_{\text{pix}}^{\text{T}}$ from Eq. 44 is 15mK for one frequency channel, which is based on the specification of the current MeerKAT survey in Table 3 and Eq. 38; to detect the cross-correlation we should find ways to reduce the $\sigma_{\text{pix}}^{\text{T}}$ as far as possible.

We first model the S/N of κ HI. We can consider the zero lag noise level for $\langle \kappa \Delta T \rangle$, i.e. where κ and ΔT are measured in the same pixel. There is no reason why the statistical noise of κ should be correlated with ΔT . The noise for the cross-correlation will therefore be proportional to the product of σ_{T} and σ_e^n , where σ_{T} is HI thermal noise which can be estimated by Eq. 44. The rms noise for weak lensing σ_e^n can be estimated by

$$\sigma_e^n = \frac{\sigma_e}{\sqrt{n_{\text{gal}}}}, \quad (45)$$

where σ_e is the variance of intrinsic galaxy ellipticities and n_{gal}

is galaxy number per pixel. For KiDS and DES-like surveys, $\sigma_e \approx 0.3$. The KiDS DR4 effective galaxy number density is $n_{\text{eff}} = 0.325 \text{ arcmin}^{-2}$ for the whole redshift range (Heymans et al. 2021; Giblin et al. 2021). For a pixel size 0.25^2 deg^2 , we find $\sigma_e^n \approx 0.03$.

The S/N of $\langle \kappa \text{HI} \rangle$ then can be estimated by

$$S/N = \frac{\sigma_{\text{HI}} \sigma_{\kappa}}{\sigma_{\text{T}} \sigma_e^n} \sqrt{N_{\text{pix}}}. \quad (46)$$

and we find that the rms lensing convergence signal σ_{κ} is similar to the rms noise σ_e^n on 0.25 deg scales (Gatti et al. 2021; Amon et al. 2022).

To estimate the signal of HI intensity mapping, we first recall that the HI brightness temperature fluctuations δT_{HI} can be expressed by:

$$\delta T_{\text{HI}} = \bar{T}_{\text{HI}}(z) b_{\text{HI}}(z) \delta_{\text{m}}(\theta, z), \quad (47)$$

where $\bar{T}_{\text{HI}}(z)$ is an average temperature over angular position (θ) for a given z and $b_{\text{HI}}(z)$ is HI bias. As the power spectrum P_{HI} is the power of the temperature fluctuation δT_{HI} , the square root of P_{HI} per volume V_{sur} is effectively the root mean square of the HI true signal (σ_{HI}),

$$\sigma_{\text{HI}} = \sqrt{P_{\text{HI}}/V_{\text{sur}}}. \quad (48)$$

We consider a survey similar to the MeerKAT pilot survey ($0.39 < z < 0.46$) over a moderately thick $\Delta z = 0.075$ redshift bin, with 0.25^2 deg^2 pixel size, $V_{\text{sur}} \sim 4000 \text{ Mpc}^3 h^{-3}$. Assuming the foregrounds and redshift space distortions have been appropriately dealt with, we can use

$$P_{\text{HI}} = \bar{T}_{\text{HI}}^2 b_{\text{HI}}^2 P_{\text{m}} \quad (49)$$

We assume an effective redshift of the survey $z_{\text{eff}} = 0.42$, $b_{\text{HI}} = 1$ and $\bar{T}_{\text{HI}} = 0.07 \text{ mK}$ (Cunnington et al. 2022; Wang et al. 2021; Santos et al. 2015). In this case, the estimation of HI rms is then

$$\sigma_{\text{HI}}(k = 0.1, z = 0.42) = 5 \mu\text{K}, \quad (50)$$

where we estimate at the $k = 0.1 \text{ h}^{-1} \text{ Mpc}$ scale. This estimation generally agrees with Table I in Santos et al. (2015) with slightly better signal rms, because Santos et al. (2015) uses smaller channel bins than the thick redshift bin we have here.

σ_{T} is approximately 15 mK for a single frequency channel given Table 3. If we stack over 200 $\Delta \nu$ channels and assume 10 hours observing time, then

$$\sigma_{\text{T}} \approx 1.1 \text{ mK}. \quad (51)$$

Then using equation (46), the estimation of S/N for κHI 2-point statistics for KiDS-like lensing surveys and MeerKAT for $k = 0.1 \text{ h}^{-1} \text{ Mpc}$ with a pixel size 0.25^2 deg^2 covering $\sim 200 \text{ deg}^2$ sky, is then

$$S/N \approx 0.24. \quad (52)$$

This means that by the current state of art, we expected to observe more instrument noise than cosmic signal from κHI cross correlations at zero lag. By including cross-correlations at different angular separations, we expect a higher total signal-to-noise.

Note that this estimation is based on the pilot survey by MeerKAT which only contains 64 dishes of 13m diameter and only observes for 10hr; for the full operation of MeerKAT or SKA-Mid, we will have more dishes, longer observation time and more frequency channels. If we assume a longer observation time such as 1000 hours (as is recommended by (Zhang et al. 2023)) and increase the number of frequency channels to 250, the estimation of σ_{MK} is then

$$\sigma_{\text{MK}}^{1000} \approx 0.01 \text{ mK}. \quad (53)$$

Table 4. Cosmological forecast from Fisher analysis including instrument noise contributions for 16-HIHI + 3- κ correlations; the uncertainties on cosmological parameters and HI bias are quoted at 95% confident level. Here we consider only HI bias model 1.

Parameters	HI bias model 1
Δh_0	± 0.28
$\Delta \Omega_{\text{m}}$	± 0.09
$\Delta \sigma_8$	± 0.32
Δn_{s}	± 0.17
$\Delta \alpha$	± 0.34

Now we have better S/N by one order of magnitude for a 3000 pixel sky. (If we use the pilot survey footprint ($\sim 200 \text{ deg}^2$), then $S/N \approx 2.4$ for zero lag.)

We confirm this calculation by generating Gaussian random fields for the instrument noise for both κ and HI fields and add these noise maps using (Eq. 44 and 45) to the simulations described in section 4. We utilise the full sky maps with NSIDE=128. The pixel number for this resolution is $N_{\text{pix}} = 196608$. Hence the estimation of S/N for this configuration is then,

$$S/N_{\text{full}}^{1000} \approx 22. \quad (54)$$

However, when we take the LoS foreground subtraction into account, the signal would be reduced by a factor of ~ 3 . This means

$$S/N_{\text{full}}^{1000} \longrightarrow \approx 7. \quad (55)$$

This estimation indicates that we would expect to observe the true signal at zero lag for 1000 hour exposure and large sky surveys such as SKA.

5.3 Fisher Analysis

We now consider the feasibility of κHI and HIHI 2-point statistics for cosmological constraints in the presence of these current noise levels. In the S/N analysis of κHI (sec. 5.2), we only considered the case where $\Delta \nu_{\text{total}} = 250 \times 0.2 \text{ MHz}$. However to compare results in sec. 4.3, we will adjust $\Delta \nu$ to match z_{HI} in Table. 1.

We generate Gaussian white noise fields for both κ and HI using the previous subsection's calculated amplitudes. We note again that in this analysis, we consider only the full-sky case. The marginalisations of cosmological parameters are illustrated by Fig. 14. Comparing this result to the no-noise case (see Fig. 11) we can see that the cosmological feasibility of HIHI and κHI are reduced significantly. We also show the resulting FoM in Fig. 15 and 2σ -constraints in Table 4. We note that the Ω_{m} constraint shows a precise estimation, although it is degenerate with α . Considering Fig. 15, we can see that the maximum of FoM when considering instrument noise is one order of magnitude less than the no-noise case (see Fig. 8). Nevertheless, all FoM plots (see Fig. 8, 9, and 15) indicate that by combining κHI likelihoods with HIHI, we can significantly enhance the feasibility of cosmological constraints from the HI intensity maps.

6 CONCLUSIONS

In this paper we have studied the 2-point statistics of lensing convergence and HI intensity mapping.

We first presented the theoretical framework for calculating

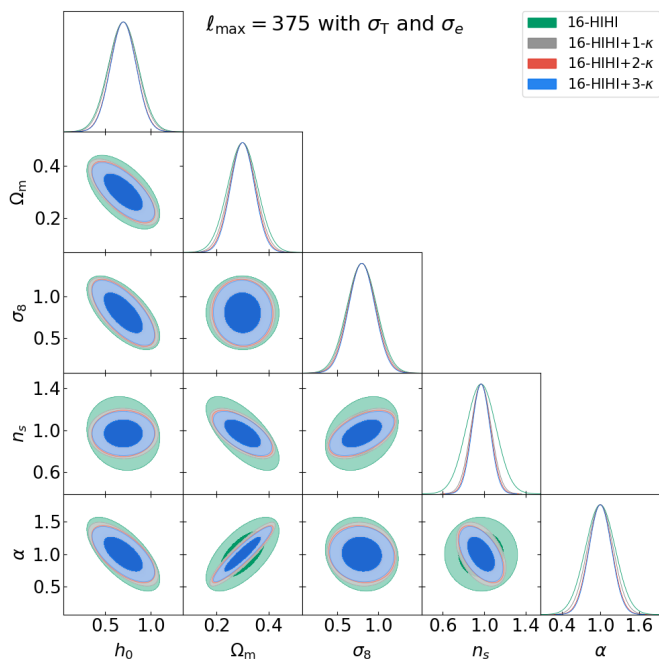


Figure 14. The likelihood contours for our multi-bin analysis with HI bias model 1 with $\ell_{\max} = 375$ for full-sky case including the instrument noise contributions; the contours show 68% and 95% confidence levels. Comparing to Fig. 11 where we ignore instrument noise contributions, we can see that h_0 is now poorly constrained.

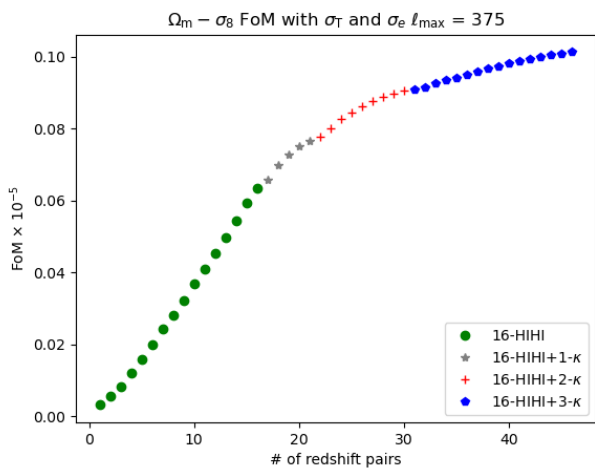


Figure 15. Figure of Merit for $\sigma_8 - \Omega_m$ constraints including instrument noise; the horizontal axis is the number of redshift bin pairs for cosmological constraints. We show cumulative FoM when including increasing numbers of HI auto-correlation redshift bins (green); then increasing numbers of cross-correlations with convergence bins (grey, red, blue). Here $\ell_{\max} = 375$. Comparing this figure to Fig. 9, we find that the FoM is lower by 1 order of magnitude.

convergence-intensity mapping cross-correlations. Next, by using realisations from an N-body simulation we have emulated HI intensity maps, and have shown that their cross-correlation with convergence maps from these simulations agree with our theoretical cross-correlation calculations.

We proceeded to study the effect of HI foreground removal on the 2-point functions. We model the effect of foreground removal by removing the mean along each line-of-sight, which effectively represents the largest radial mode. From our HI maps, following the method of [Cunnington et al. \(2019b\)](#). We then measure the post-removal cross-power; we find that the foreground removal modestly reduces the κ HI power spectrum signal, by a factor $A_{\text{clean}}(z_{\text{HI}}, z_{\kappa}, z_{\text{max}})$. In the case of forthcoming HI experiments that will measure HI at $z_{\text{max}} < 1$, $A_{\text{clean}}(z_{\text{HI}} < 0.5, z_{\kappa} = 0.78, z_{\text{max}} = 1)$ is approximately 2.5 for our catalogues.

In the following section, we utilised the Fisher matrix formalism to forecast best-case cosmological constraints for the convergence-HI probe, for the maximal case of full sky and subdominant telescope noise, but while including foreground removal. We calculated the Fisher matrix for $\kappa\kappa$, HIHI and κ HI 2-point functions by using the measured covariance matrices from Sec 3.

We find that a single redshift slice of the HI intensity map and κ can constrain cosmological parameters for known bias (see Fig. 7), but when b_{HI} is a further parameter (or several), the few-slice 3×2 point functions do not sufficiently constrain the cosmological parameters compared to current cosmological surveys such as Planck and DES ([Planck Collaboration et al. 2018](#); [Abbott et al. 2019](#)).

Hence, several cross-bin correlations are required in order for this probe to be of interest. In Sec 4.3, we have explored the use of several redshift bins for HI and convergence, together with the effect of b_{HI} on cosmological constraints. We consider both the current state of art where $\ell_{\max} < 400$, and the futuristic case where $\ell_{\max} > 1000$. Both cases show that a set of 2-point functions constrain the uncertainty in cosmological parameters to a comparable level with current experiments. All FoMs show that by including the cross-correlation of a lensing survey with the 21cm signal, we can improve the HI auto constraints.

We then examined the impact of a cut-sky survey. In this analysis, we evaluated the 2-point statistics based on a 300 deg^2 observed patch of sky. Due to the statistical incompleteness, detecting cosmic signals becomes marginal in this context.

In sec. 5.1, we explore the instrument noise affecting lensing and HI galaxy surveys. The thermal noise of a single-dish survey was calculated. In this study, we focus on instruments similar to MeerKAT for radio observations and KIDs-like surveys for optical counterparts. Our analysis demonstrates the feasibility of detecting the κ HI cross-correlation, provided we have sufficient sky coverage and long exposure times for the radio measurements.

Even though we have shown positive results for 2-point statistics between the κ field and HI intensity map, there are important caveats that remain to be explored further:

- In this study we have created HI intensity maps based on the assumption that they are linearly biased in relation to overdensity δ_m . A more realistic study should construct HI intensity maps by assigning HI mass M_{HI} to simulated halo catalogues. Also in future work the generated HI maps will be compared in detail to real data.
- We have approximated the foreground cleaning by removing the mean fluctuation along the line of sight, which effectively represents the largest radial mode. More detailed emulation of the foreground cleaning will be studied in future.
- The cosmological and b_{HI} constraint predictions have been

obtained by using the idealised Fisher matrix analysis; for real data, Markov Chain Monte Carlo methods are required to deal with non-Gaussian likelihoods and realistic degeneracies between parameters.

- Only the Λ CDM model is considered in these parameter constraints. Further extensions (e.g. wCDM) should be considered in further work.

- Only 2-point statistics have been explored in this research. However the study by Schmit et al. (2019) shows that combining the bispectrum and power spectrum can reduce the error of cosmological parameters by an order of magnitude compared to Planck.

- This study has only explored the low-redshift 2-point functions. The high redshift probes at the time of the Epoch of Reionization and the Cosmic Microwave Background are not taken into account. It is an interesting matter for future work to consider whether 2-point statistics between the EOR HI and CMB weak lensing can also be measured.

In conclusion, κ -HI cross-correlations are an intriguing additional probe for cosmology, which are not destroyed by foreground removal. This probe will be available for measurement with forthcoming HI and lensing surveys this decade.

ACKNOWLEDGEMENTS

We acknowledge studentship support from the Thai Royal Government for AS. We thank Tzu-Ching Chang (JPL), Yu-Wei Liao (ASIAA), Steve Cunnington (University of Manchester) and Utane Sawangwit (National Astronomical Research Institute of Thailand) for extremely helpful discussions. DB was supported by STFC Consolidator Grant ST/S000550/1. Calculations were made using Chanlwan High Performance Computer at the National Astronomical Research Institute of Thailand.

DATA AVAILABILITY

In this work we use the N-Body simulations and weak lensing catalogues from Takahashi et al. (2017). The catalogues can be obtained at http://cosmo.phys.hirosaki-u.ac.jp/takahashi/allsky_raytracing. The measured 2-point functions and Python codes for calculations in sections 3 and 4 are available in Github, at <https://github.com/AnutUoP/2020s-KappaHI>. Other data will be shared on reasonable requests to the corresponding author.

REFERENCES

Abbott T. M. C., et al., 2018, *Phys. Rev. D*, **98**, 043526
 Abbott T. M. C., et al., 2019, *Astrophys. J.*, **872**, L30
 Alam S., et al., 2017, *MNRAS*, **470**, 2617
 Alonso D., Sanchez J., Slosar A., LSST Dark Energy Science Collaboration 2019, *MNRAS*, **484**, 4127
 Amon A., et al., 2022, *Phys. Rev. D*, **105**, 023514
 Bartelmann M., Schneider P., 2001, *Phys. Rep.*, **340**, 291
 Battye R. A., et al., 2013, *MNRAS*, **434**, 1239
 Baxter E. J., et al., 2019, *Phys. Rev.*, **D99**, 023508
 Bigot-Sazy M.-A., et al., 2015, *Monthly Notices of the Royal Astronomical Society*, **454**, 3240
 Blake C., Glazebrook K., 2003, *ApJ*, **594**, 665
 Brown M. L., Castro P. G., Taylor A. N., 2005, *MNRAS*, **360**, 1262
 Bull P., Ferreira P. G., Patel P., Santos M. G., 2015, *ApJ*, **803**, 21
 CHIME Collaboration et al., 2022, arXiv e-prints, p. [arXiv:2202.01242](https://arxiv.org/abs/2202.01242)
 Castro P. G., Heavens A. F., Kitching T. D., 2005, *Phys. Rev. D*, **72**, 023516
 Chapman E., et al., 2012, *MNRAS*, **423**, 2518

Cunnington S., Harrison I., Pourtsidou A., Bacon D., 2019a, *MNRAS*, **482**, 3341
 Cunnington S., et al., 2019b, *MNRAS*, **488**, 5452
 Cunnington S., Pourtsidou A., Soares P. S., Blake C., Bacon D., 2020, *MNRAS*, **496**, 415–433
 Cunnington S., et al., 2022, arXiv e-prints, p. [arXiv:2206.01579](https://arxiv.org/abs/2206.01579)
 Cunnington S., et al., 2023, *MNRAS*, **523**, 2453
 Euclid Collaboration 2019, arXiv e-prints, p. [arXiv:1910.09273](https://arxiv.org/abs/1910.09273)
 Fang X., Eifler T., Schaan E., Huang H.-J., Krause E., Ferraro S., 2022, *MNRAS*, **509**, 5721
 Feldman H. A., Kaiser N., Peacock J. A., 1994, *ApJ*, **426**, 23
 Fernandez-Soto A., Lanzetta K. M., Chen H.-W., Pascarella S. M., Yahata N., 2001, *The Astrophysical Journal Supplement Series*, **135**, 41
 Gatti M., et al., 2021, *MNRAS*, **504**, 4312
 Giblin B., et al., 2021, *A&A*, **645**, A105
 Górski K. M., et al., 2005, *ApJ*, **622**, 759
 Harker G., et al., 2010, *MNRAS*, **405**, 2492
 Heavens A., 2003, *MNRAS*, **343**, 1327
 Heymans C., et al., 2021, *A&A*, **646**, A140
 Hinshaw G., et al., 2013, *ApJS*, **208**, 19
 Hivon E., Górski K. M., Netterfield C. B., Crill B. P., Prunet S., Hansen F., 2002, *ApJ*, **567**, 2
 Hu W., Jain B., 2004, *Phys. Rev.*, **D70**, 043009
 Kamionkowski M., Smith T. L., Heavens A., 2011, *Phys. Rev. D*, **83**, 023007
 Kim J., 2011, *A&A*, **531**, A32
 Kim J., Naselsky P., 2010, *A&A*, **519**, A104
 Lewis A., Bridle S., 2002, *Phys. Rev. D*, **66**, 103511
 LoVerde M., Afshordi N., 2008, *Phys. Rev. D*, **78**, 123506
 Mao Y., et al., 2008, *Phys. Rev. D*, **78**, 023529
 Martin A. M., Giovanelli R., Haynes M. P., Guzzo L., 2012, *The Astrophysical Journal*, **750**, 38
 Mendez R. A., Silva J. F., Oróstica R., Lobos R., 2014, *PASP*, **126**, 798
 Padmanabhan H., Refregier A., Amara A., 2020, *MNRAS*, **495**, 3935–3942
 Pandey S., et al., 2021, arXiv e-prints, p. [arXiv:2105.13545](https://arxiv.org/abs/2105.13545)
 Planck Collaboration et al., 2018, arXiv e-prints, p. [arXiv:1807.06205](https://arxiv.org/abs/1807.06205)
 Platania P., Bensadoun M., Bersanelli M., De Amici G., Kogut A., Levin S., Maino D., Smoot G. F., 1998, *ApJ*, **505**, 473
 Pourtsidou A., 2017, arXiv e-prints, p. [arXiv:1709.07316](https://arxiv.org/abs/1709.07316)
 Pourtsidou A., Bacon D., Crittenden R., 2017, *MNRAS*, **470**, 4251
 Pratten G., Munshi D., Valageas P., Brax P., 2016, *Phys. Rev. D*, **93**, 103524
 Santos M. G., Ferramacho L., Silva M. B., Amblard A., Cooray A., 2010, *MNRAS*, **406**, 2421
 Santos M., et al., 2015, in *Advancing Astrophysics with the Square Kilometre Array (AASKA14)*, p. 19 ([arXiv:1501.03989](https://arxiv.org/abs/1501.03989))
 Schmit C. J., Heavens A. F., Pritchard J. R., 2019, *MNRAS*, **483**, 4259
 Seo H.-J., Dodelson S., Marriner J., McGinnis D., Stebbins A., Stoughton C., Vallinotto A., 2010, *ApJ*, **721**, 164
 Shaw J. R., Sigurdson K., Pen U.-L., Stebbins A., Sitwell M., 2014, *The Astrophysical Journal*, **781**, 57
 Smoot G. F., Debono I., 2017, *A&A*, **597**, A136
 Spinelli M., Bernardi G., Santos M. G., 2018, *MNRAS*, **479**, 275–283
 Spinelli M., Carucci I. P., Cunnington S., Harper S. E., Irfan M. O., Fonseca J., Pourtsidou A., Wolz L., 2022, *MNRAS*, **509**, 2048
 Square Kilometre Array Cosmology Science Working Group et al., 2020, *Publ. Astron. Soc. Australia*, **37**, e007
 Su H., et al., 2018, *MNRAS*, **479**, 4041–4055
 Switzer E. R., et al., 2013, *MNRAS: Letters*, **434**, L46–L50
 Takahashi R., et al., 2012, *ApJ*, **761**, 152
 Takahashi R., et al., 2017, *ApJ*, **850**, 24
 Tegmark M., Taylor A. N., Heavens A. F., 1997, *ApJ*, **480**, 22
 The CHIME Collaboration et al., 2022, arXiv e-prints, p. [arXiv:2201.07869](https://arxiv.org/abs/2201.07869)
 Tröster T., et al., 2022, *A&A*, **660**, A27
 Upham R. E., Whittaker L., Brown M. L., 2019, *MNRAS*, **491**, 3165–3181
 Wang J., et al., 2021, *MNRAS*, **505**, 3698
 Wolz L., Tonini C., Blake C., Wyithe J. S. B., 2016, *MNRAS*, **458**, 3399
 Wuensche C. A., the BINGO Collaboration 2019, in *Journal of Physics Conference Series*, p. 012002 ([arXiv:1803.01644](https://arxiv.org/abs/1803.01644)), doi:10.1088/1742-6596/1269/1/012002

Zhang M., Li Y., Zhang J.-F., Zhang X., 2023, [MNRAS](#), 524, 2420

This paper has been typeset from a $\text{\TeX}/\text{\LaTeX}$ file prepared by the author.